

# Magnetohydrodynamic Energy Harvester for Low-Power Pipe Instrumentation

Xiaotong Zhang<sup>✉</sup>, Graduate Student Member, IEEE, and Kamal Youcef-Toumi, Senior Member, IEEE

**Abstract**—Smart pipes can be adopted as a solution to problems in water distribution systems. However, the real application of such a system is usually constrained by power delivery. In this article, a magnetohydrodynamic (MHD) energy harvester for low-power pipe instrumentation is developed. A theoretical model of the maximum power output containing parameters of water conductivity, flow velocity, magnetic flux density, and water channel volume is derived. To enhance the magnetic flux density, a magnetic concentrator is designed and carefully tuned to arrange the magnetic flux as we desire and magnify the magnetic flux density within the channels. A spiral flow diverter is proposed to reconfigure the original pipe flow pattern and divert the flow into the surrounding channels to enhance the flow velocity. After integrating the proposed improvements from different fields and globally optimizing the power output, a final design is prototyped and tested in the lab, which achieves a maximum power output of 87.47 nW with a 2-m/s pipe inlet velocity. To the best of our knowledge, this is the first MHD energy harvester for low-power sensor networks. Its great potential is demonstrated, and several potential enhancements to the power output are proposed and analyzed.

**Index Terms**—Energy harvester, magnetic concentrator, magnetohydrodynamics (MHD), smart sensor networks, spiral flow.

## I. INTRODUCTION

WATER is one of the most important resources on earth. Water dramatically influences human civilization in the way of health and pollution, agriculture, hygiene, transportation, fire considerations, recreation, industrial application, etc. Moreover, no creatures can live without water.

However, the water distribution system heavily relied on by modern civilization introduces severe problems, which can result in significant resource waste, safety issues, and infrastructure damage. In 2013, 14–18% of the clean drinkable water distributed through water distribution pipe systems was leaked into the United States ground, which is estimated to be about

Manuscript received 23 September 2021; revised 15 January 2022; accepted 6 March 2022. Date of publication 22 April 2022; date of current version 14 December 2022. This work was supported by MathEarth Inc. Recommended by Technical Editor J. Zhao and Senior Editor Y. Li. (*Corresponding author: Xiaotong Zhang.*)

The authors are with the Department of Mechanical Engineering, Massachusetts Institute of Technology, Cambridge, MA 02139 USA (e-mail: kevxt@mit.edu; youcef@mit.edu).

Color versions of one or more figures in this article are available at <https://doi.org/10.1109/TMECH.2022.3164340>.

Digital Object Identifier 10.1109/TMECH.2022.3164340

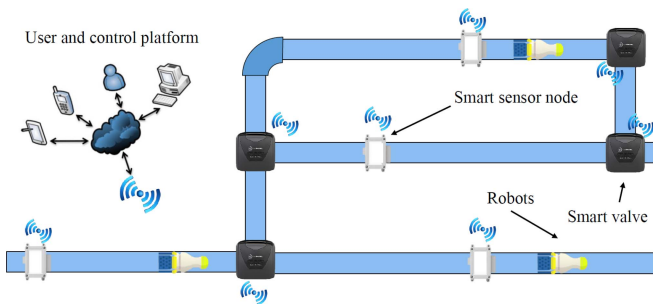


Fig. 1. Example of instrumented pipe systems.

2.1 trillion gallons of water [1]. When the scope is zoomed out to our blue globe, the severity of water leak is different in every region, and the percentage varies from 5% in Japan [2] to more than 50% in some least developed countries [3], [4]. As a result, the annual economic loss for water companies around the world adds up to \$14 billion [5]. In addition to economic loss, the underground water leak can also cause contamination in water [6], horrendous infrastructure destruction [7], and even human casualties.

Instrumented pipes can significantly reduce such water pipe system problems. Most of these pipe system problems can be avoided if they can be discovered and solved in an early stage [8]. Thus, a very likely solution is to adopt instrumented pipe systems to monitor and forecast the working condition of the system and perform self-control and self-recovery. An example is illustrated in Fig. 1, which is developed based on and inspired by the work in [9] after further integrating smart valves and robots for leak detection and repair. Cutting-edge sensor nodes perform real-time data acquisition [10], [11] and communication with distributed smart agents and/or a centralized management and control center [12]. When an anomaly is detected or predicted, a solution is generated and executed locally through flow control valves, robots, and any other agents [13]. This system can effectively monitor the integrity of the asset, predict future problems, and recover automatically without human intervention.

However, the power delivery constraint to the wireless sensors limits the deployment of instrumented pipe systems in real applications. These sensors are usually hard to reach, densely distributed, and an ultralong lifetime is required. These characteristics prohibit the use of traditional power delivery mechanisms, such as batteries and some existing energy harvesting methods for other applications. It is worth noting that the average pipe lifetime in the United States is 125 years [14].

Energy harvesting researchers have explored different materials and principles. Turbines, converting the longitudinal flow momentum into rotational movement of the blades, are the most popular harvesters in this area, usually with a more than sufficient power output [15]. Besides turbines, significant research has focused on piezoelectric materials [16]–[18] and direct electromagnetic interaction [19] for harvesting the energy of mechanical vibrations stimulated by inherent turbulence phenomenon, e.g., vortex induced vibration and Karman vortex street. However, all these three methods require mechanically moving or vibrating components, which limit the lifetime of these energy harvesters. Moreover, piezoelectric material and direct electromagnetic interaction also suffer greatly from off-resonance behavior, which constrains the working flow velocity [20]. Other options include thermoelectricity [21] and solar [22] based energy harvesters. However, the power output of thermal electricity is dramatically confined by the limited temperature difference. When it comes to solar energy, placing such cells above ground will consume additional space and can require complicated wiring.

Ultralow-power sensors with lower and lower power requirements have been proposed, analyzed, fabricated, and tested. The power requirement of microcontrollers, strain gauges, microphones, pressure sensors, temperature sensors, bluetooth, etc., have been dramatically reduced [20], [23]–[25]. As a result, in 2014, a new leak detection sensor node was proposed and developed [9]. Enhanced by advanced power management strategies, the sensor is turned ON every six hours and achieves a power requirement of as low as  $2.2 \mu\text{W}$ . After adopting a more aggressive power management strategy and microelectromechanical systems (MEMS) technology, the power requirement can be further reduced to hundreds of nanowatts.

Magnetohydrodynamics (MHD) has great potential in energy harvesting for water pipe applications. In 1832, Michael Faraday conducted an experiment in London trying to measure the voltage difference between the two river banks caused by the interaction between the flow field and the earth's magnetic field. However, the current was too small for the equipment to measure at that time [26]. In the 20th century, several countries successfully developed MHD energy harvesters using plasma as a conductor [27]. Since then, more research on MHD flow structure and precise numerical models has been conducted [28]–[30]. All these works have increased our understanding of MHD. This type of energy harvester has several unique advantages, which are very difficult for existing energy harvesting methods to compete with.

**1) No Moving Mechanical Part:** Unlike traditional turbines, piezoelectricity, and direct electromagnetics, there is no moving mechanical part, so the lifetime is dramatically increased.

**2) Wide Working Range:** It can work under any regular flow velocity because it does not suffer from off-resonance, which is a common and severe problem for piezoelectricity and electromagnetics. Unlike solar energy, this MHD energy harvester does not require above-ground space. Unlike thermal electricity, it works under any normal temperature in water pipes.

**3) Direct Current Output:** The current and voltage output from MHD energy harvesters is direct current, which means

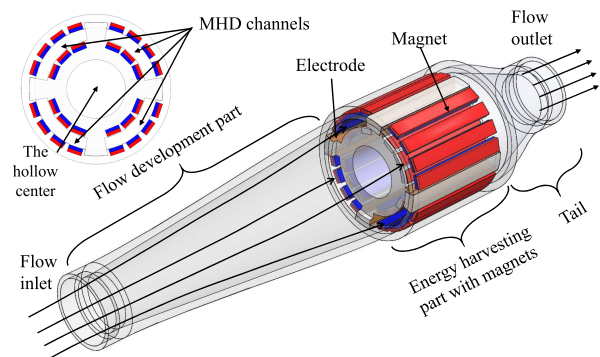


**Fig. 2.** Conceptual design with its cross section of the energy harvesting part. The gold surfaces are the electrodes and the blocks in red and blue are the magnets. The hollow center is to allow in-pipe robots to navigate through and reduce flow blockage. The MHD channels are the channels for MHD to work.

that rectifiers can be much easier and even removed if the flow velocity is constant.

This article focuses on the MHD phenomenon. Specifically, we will investigate its potential to deliver sufficient power to wireless sensor nodes. Theoretical analysis, physics-based modeling, numerical simulation, and experiments are presented. The contribution of this article can be summarized as follows: 1) the idea and development of a novel MHD energy harvester using permanent magnets working with clean water. To the best of our knowledge, this is the first working MHD energy harvester aimed at powering ultralow-power sensor nodes; 2) a systematic design and optimization methodology; 3) two strategies to enhance power output, namely a magnetic concentrator and a spiral flow diverter to amplify magnetic flux density and flow velocity, respectively.

The rest of this article is organized as follows. In Section II, we briefly describe the conceptual design of the energy harvester. Section III presents the working principle and a simplified model for MHD, which directs our following design and optimization. Section IV presents the optimization of the magnetic field and flow field. In Section V, a final design is proposed along with a prototype. The experimental setup, experimental results, as well as discussions, are covered in Section VI. Finally, Section VII concludes this article.

## II. CONCEPTUAL DESIGN

A conceptual design is illustrated in Fig. 2. The design consists of three parts: 1) a flow development part to allow the original pipe flow to better expand; 2) an energy harvesting part with permanent magnets and electrodes for MHD to work as desired; 3) a tail part to confine the flow to the size of the pipe and alleviate flow blockage. The center of the energy harvesting part is hollow to significantly reduce the pressure drop caused by the harvester. In the meantime, the hollow center can allow in-pipe robots [31] to navigate through. Thus, the channel for MHD to work is placed around the hollow center and separated into four subchannels by the electrodes. With the help of the flow development part, the inlet flow is expanded and separated into the four channels, as shown in Fig. 2. The MHD energy

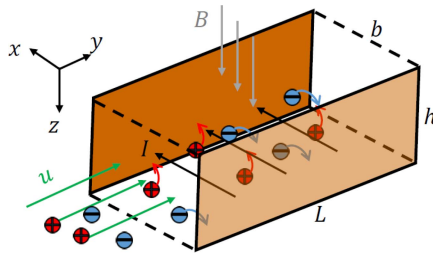


**Fig. 3.** MHD principle with a channel of length  $L$ , height  $h$ , and width  $b$ . The flow velocity is  $u$ ,  $B$  is the magnetic flux density, and  $I$  is the resultant current.

harvester can be installed as a separate and additional section on the original pipe networks or integrated directly and seamlessly on the newly built smart pipes.

### III. MHD PRINCIPLE AND MODELING

#### A. Conductivity of Water

Conductivity is the macroscopical reflection of the existence of ionic content in a solution. Even in ultrapure water, the autodissociation process of water will endow the water with a very low electric conductivity of  $5.5 \times 10^{-6}$  S/m at the temperature of 25 °C [32]. With ionized impurities in water, such as sulfate, calcium, chloride, and sodium, the electric conductivity can be dramatically increased. The conductivity of tap water in our lab is measured to be 0.0750 S/m, while the conductivity of seawater can be more than 1 S/m [33]. The existence of these ions is the prerequisite for MHD to work.

#### B. MHD Principle Modeling

Fig. 3. is a simplified MHD energy harvester to help to illustrate the principle. Current  $I$ , flow velocity  $u$ , and magnetic flux density  $B$  are in the direction of  $x$ ,  $y$ , and  $z$  direction, respectively. The channel walls perpendicular to the  $x$  axis are attached with conductive electrodes. In the presence of the magnetic field, moving positive and negative charges in the water driven by the flow will be subjected to an additional Lorentz force pointing in the opposite direction, according to

$$F = q(E + u \times B) \quad (1)$$

where  $q$  is the charge;  $E$  is the electric field strength;  $u$  is the velocity of the charge; and  $B$  is the magnetic flux density. Positive and negative charges will tend to move in the opposite direction, which induces a current. On the other hand, Ohm's law takes the general form of

$$J = \sigma(E + u \times B) \quad (2)$$

where  $J$  is the current density, and  $\sigma$  is the conductivity of water. Given the relationships for the current  $I$ ,  $I = j_x h L$ , and the internal e.m.f.  $V_x$ ,  $V_x = E_x b = I(R_{\text{load}} + r)$ , where  $r$  is the internal resistance, and  $R_{\text{load}}$  is the external load resistance, the current output in an external circuit can be derived as

$$I = \frac{\sigma h L b u B}{2b + \sigma h L R_{\text{load}}} \quad (3)$$

which easily leads to the power output extracted by the external load resistance

$$P_{\text{out}} = \left( \frac{\sigma h L b u B}{2b + \sigma h L R_{\text{load}}} \right)^2 R_{\text{load}}. \quad (4)$$

After simple rearrangement and calculation, the max power output can be found as

$$P_{\text{out}_{\max}} = \frac{1}{8} \sigma V B^2 u^2 \quad (5)$$

where  $V$ , the volume of the flow channel of Fig. 3, is defined as  $V = b h L$ . The optimal load resistance is

$$R_{\text{load}} = \frac{2b}{\sigma h L}. \quad (6)$$

It is worth noting that (5) is the maximum power that can be extracted and consumed by the external load resistance. The maximum of the total generated power will be two times that of (5).

#### C. MHD Model Analysis

From the above expressions, it is clear that the magnetic flux density  $B$  and flow velocity  $u$  are fully decoupled, although the relationship is not linear. Both magnetic flux density  $B$  and flow velocity  $u$  have a quadratic contribution to the final results, which means that more weight and effort can be made in the optimization of these two fields.

Significant works have been conducted and archived on theoretical modeling, numerical simulation methods, and experimental studies on static magnetic field analysis and hydrodynamics. However, whether these methods and approaches can be applied to MHD energy harvesters still requires careful analysis.

The governing equations of MHD flow can be summarized as a mass continuity in (7) and a Cauchy momentum in (8).

$$\frac{\partial \rho}{\partial t} + \nabla \cdot (\rho u) = 0 \quad (7)$$

$$\rho \left( \frac{\partial}{\partial t} + u \cdot \nabla \right) u = J \times B - \nabla p \quad (8)$$

where  $\rho$  is the density of water, and  $p$  is the pressure. The only difference after considering MHD is the term  $J \times B$  representing the additional Lorentz force acting on the control volume, which is added on the right side of (8). The pressure gradient term for the pipe flow can be calculated as

$$\nabla p = f \frac{1}{D} \frac{\rho u_{\text{avg}}^2}{2} \quad (9)$$

where  $D$  is the diameter of the pipe,  $f$  is the Darcy friction factor, and  $\rho u_{\text{avg}}^2$  is the dynamic pressure. However, in our application, where the current density and the magnetic flux density generated by the permanent magnets are much lower than those of an MHD energy harvester used in a large plant with plasma as a working substance, the additional Lorentz force term is negligible when compared with the pressure gradient term. Thus, in the following analysis, principles and results from other general hydrodynamics or fluid mechanics research can be

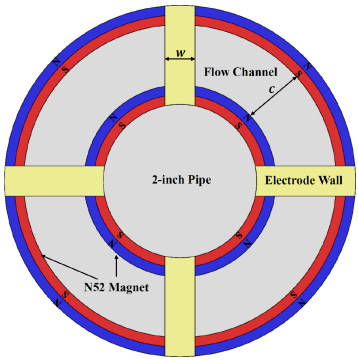


**Fig. 4.** Cross section of the energy harvesting part in the conceptual design.

applied. Well-developed simulation methods are also suitable, which makes the design and analysis much easier and efficient.

Similarly, for the static magnetic field, the current density term in Ampere's circuit law is neglected. Thus, the MHD effect can also be set aside when analyzing the magnetic field.

#### IV. DESIGN AND OPTIMIZATION

In this section, analysis and design methods are proposed to improve the power output by enhancing the magnetic flux density and the flow velocity.

##### A. Magnetic Field Analysis and Optimization

Amplifying the net magnetic flux density in the channels is a challenge. This is mainly due to the inherent characteristics of magnetic field lines. The channels in the conceptual design will also be occupied with magnetic flux in the opposite direction, which is not desired. In Fig. 4, each channel is made up of two N52 degree arc Neodymium magnets, two electrodes, and an arc space for the flow to move through. Because the total net magnetic flux for any arbitrary closed control volume must be zero, the net magnetic flux in the channel will equal the net opposite magnetic flux within the electrode walls, which is very small.

An effective way to eliminate this problem is to introduce a magnetic concentrator with high magnetic permeability to guide the magnetic flux in the way we desire. The concentrator proposed is shown in Fig. 5 with cyan color. With this design, most of the opposite magnetic flux starts from the north pole of the outer arc magnets, keeps traveling in the concentrator through the outer circular loop, the straight channel walls, and the inner circular loop, and finally, arrives at the south pole of the inner magnets. Thus, the net magnetic flux density in the channel will be amplified.

Numerical simulation is conducted to validate the performance of the concentrator and study the influence of several parameters. Table I shows how the factor values vary in the different simulations. Relative permeability  $\mu_r$  controls how attractive the concentrator is to the magnetic flux. The saturation magnetic flux density  $B_s$  controls the saturation point of the material, reflecting the amount of magnetic flux the material can

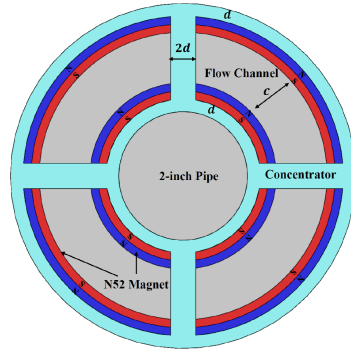


**Fig. 5.** Cross section of the energy harvesting part with the magnetic concentrator.

**TABLE I**  
PARAMETER VALUES IN SIMULATIONS

	Factor	Comment
Material	METGLAS 2714A	$\mu_r = 1 \times 10^6, B_s = 0.57T$
	Mu-metal	$\mu_r = 5 \times 10^5, B_s = 0.75T$
	Ductile Iron	$\mu_r = 2 \times 10^3, B_s = 1.80T$
Channel width c	5 mm - 30 mm with an interval of 5 mm	Distance between two layers of magnets
Loop width d	1 mm - 15 mm with an interval of 2 mm	The width of the circular part

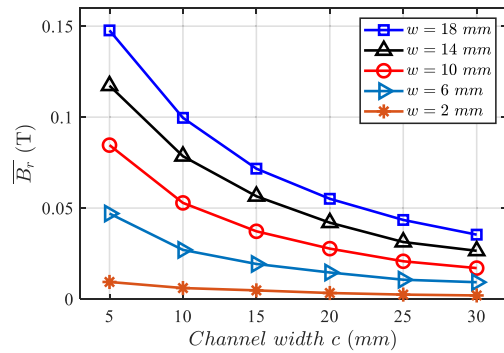


**Fig. 6.** Mean magnetic flux density in the radial direction  $\overline{B_r}$  without the magnetic concentrator for various channel width c and wall distance w.

hold within itself. Higher values of these two factors are usually better. However, most materials present a tradeoff between its  $\mu_r$  and  $B_s$ , which requires us to analyze the effect of these factors and find the optimum. Another two factors are geometrical factors, the channel width c, and the loop width d.

The simulation for the static magnetic field is performed using ANSYS Workbench 2019 R2. With the help of the parameter space and its automatic execution function in ANSYS, all combinations of the factor values are simulated automatically.

The effect of the magnetic concentrator is verified first. The simulation results without the magnetic concentrator are plotted in Fig. 6. And it is clearly shown that the magnetic flux density in the channels is very small. The mean magnetic flux density in the radial direction  $\overline{B_r}$  increases with the wall distance w, which agrees well with our analysis and prediction. And  $\overline{B_r}$  decreases with channel width c, which means that the magnetic flux density field is very sensitive to the distance between magnets. After

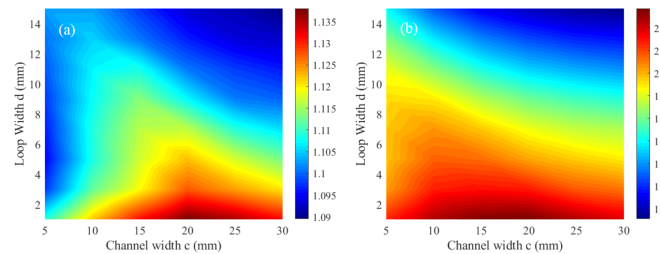


Fig. 7. Contour plots of (a)  $\frac{B_r_{\text{Mu-metal}}}{B_r_{\text{MATGLAS}}}$ ; (b)  $\frac{B_r_{\text{Iron}}}{B_r_{\text{MATGLAS}}}$ .

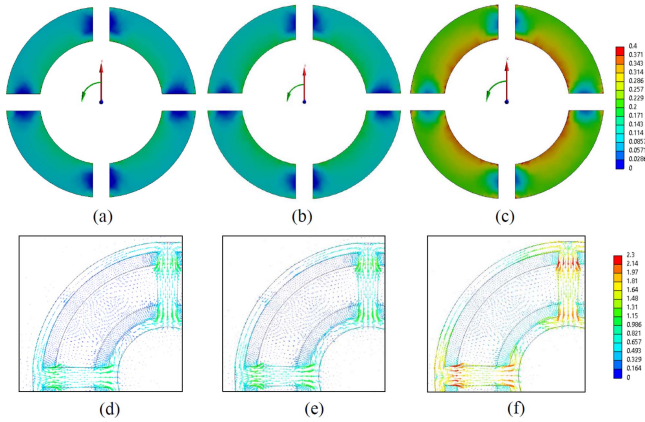


Fig. 8. Contour plots of magnetic flux density with the material of (a) METGLAS 2714 A; (b) mu-metal; (c) iron. Magnetic flux vector plots with the material of (d) METGLAS 2714 A; (e) mu-metal; (f) iron.

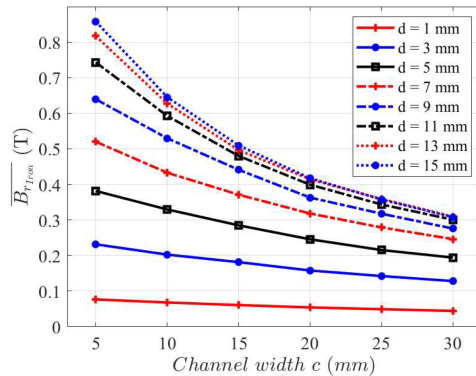


Fig. 9.  $\frac{B_r_{\text{Iron}}}{(T)}$  with different sizes and configurations.

comparing with the results in Fig. 9, the amplification of the magnetic flux density is verified.

The influence of different concentrator materials is then analyzed. In Fig. 7, the ratios of the magnetic field with different materials under various same geometrical parameter combinations are shown. A ratio greater than one means that the material on the numerator is better than the one in the denominator. It can be concluded that, within the geometrical parameter space for this application, mu-metal performs better than MATGLAS 2714 A and ductile iron performs better than mu-metal. Thus, in this application, a material with a high saturation point is more desirable.

The reason for this phenomenon can be drawn from Fig. 8. All these three materials have relatively high permeability compared with water and air. Thus, they all tend to attract lots of magnetic flux. However, because of the high magnetic saturation point, the magnetic flux density in iron is much larger than the two other materials. Thus, iron material contains much more opposite magnetic flux, and the net magnetic flux density in the channel region is dramatically amplified. From another point of view, because the size of the magnetic concentrator cannot be large enough, all three materials saturate. In this case, the saturation point will be the key factor influencing its performance the most.

Next, our analysis on the form and size will be based on materials with a high saturation point but moderate relative permeability. We will take iron as an example. Results of average magnetic flux density in radial direction with different  $c$  and  $d$  are plotted in Fig. 9.

The simulation results agree well with our analysis. Larger  $c$  will allow more space to place more magnets, but the magnetic flux density between two layers of magnets is very sensitive to the distance. Thus, the overall effect will make  $\frac{B_r_{\text{Iron}}}{(T)}$  decrease with  $c$ . When it comes to the loop width  $d$ , larger  $d$  enhances  $\frac{B_r_{\text{Iron}}}{(T)}$  because it will allow more magnets to be installed, and it can contain more opposite magnetic flux. However, the trend is almost converged when  $d \geq 11$  mm, which means that saturation is not the dominant factor anymore. The benefit in increasing further the value of  $d$  is limited. Moreover, the influence of  $d$  on the flow field is assumed to be trivial because  $d$  influences the position of the channels the most, which is not the key factor for the flow field. Therefore, the  $d$  value can be determined to be 11 mm after balancing the performance and the overall size of the energy harvester in this application to avoid bulky devices in real deployment. However, the value of  $c$  has to be determined after the analysis of the flow field because different  $c$  will dramatically influence the channel flow field, given the strong boundary effect.

### B. Flow Field Analysis and Optimization

Three-dimensional numerical simulation of the flow field is performed using the FLUENT module in the ANSYS Workbench 2019 R2 platform. And a significant problem when we analyze the conceptual design is that the pattern of the original pipe flow is too strong in the flow development part of Fig. 2. Thus, only a small amount of the flow is expanded, and the flow velocity in the channel is relatively small. To solve this problem, we develop a spiral flow diverter to enhance the flow velocity in the channels. Its working principle and results directly related to the performance of the MHD energy harvester are briefly described in this section.

The flow velocity profile of a Rankine vortex is described as

$$u_\theta(r) = \begin{cases} \Gamma r / (2\pi R^2) & r \leq R \\ \Gamma / (2\pi r) & r > R \end{cases} \quad (10)$$

where  $u_\theta$  is the tangential velocity,  $R$  is the radius of the vertex,  $\Gamma$  is the circulation, and  $r$  is the distance between a specific point and the center of the vertex. According to this Rankine vortex model, inside the region of the vortex, flow velocity in

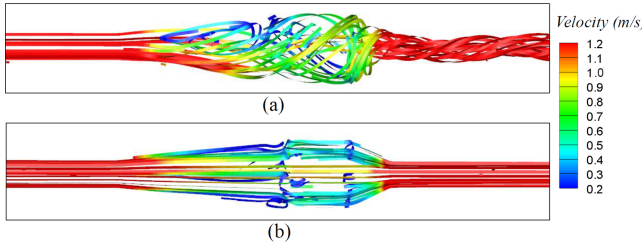


**Fig. 10.** Streamline plots with 2-m/s inlet velocity for (a) spiral channels with width = 20 mm, pitch = 400 mm; (b) the case without a spiral flow diverter.

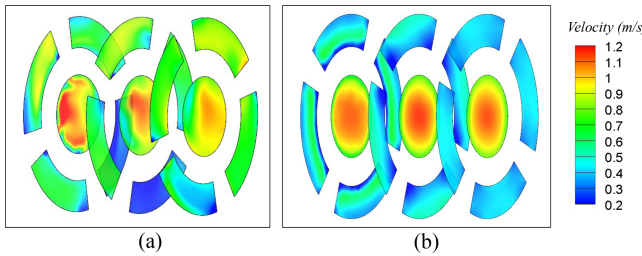


**Fig. 11.** Velocity contour with 2-m/s inlet velocity on three slices in the harvester section for (a) spiral channels with width = 20 mm, pitch = 400 mm; (b) the case without a spiral flow diverter. The three slices are located at the very front, middle, and very end of the energy harvesting part.

the region with larger radial displacement from the center is increased. And the working channels in our design are placed far from the middle to reduce blockage in the pipe flow. Therefore, an artificially induced vortex will be beneficial.

With this idea in mind, the straight working channel is transformed to be spiral. A spiral flow guide with a gradually changing pitch is augmented in the flow development part of the conceptual design. And the transition between the flow development part and the energy harvesting part is made to be smooth to reduce the blockage on flow.

The effect of this spiral flow diverter is verified with 3-D numerical simulation. The numerical methods adopted are the same as those in [34], which has verified that the numerical setup is sufficiently accurate when simulating spiral flow within a confined space. The end time in the simulation is set to be 25 s for the mean value of flow velocity in all the cases to converge. The streamline comparison in Fig. 10 clearly shows that the proposed flow diverter can induce the vortex, which agrees with our analysis. And the flow velocity contour in Fig. 11 indicates that the average flow velocity in the channels is amplified, while the velocity in the hollow center area is reduced.

The pitch of the spiral flow channel, channel width  $c$ , and inlet flow velocity are varied in the series simulations. To avoid the strong influence of boundary effects, the values of  $c$  should not be smaller than 10 mm. The plot of average flow velocity  $\bar{v}_{mag}$  in Fig. 12(a) shows that when channel width  $c = 20$  mm, all the cases with the spiral flow diverter performs better than the cases without the spiral diverter.  $\bar{v}_{mag}$  decreases with the channel width  $c$  and the spiral channel pitch. However, the influence of pitch on the performance is much more limited when compared

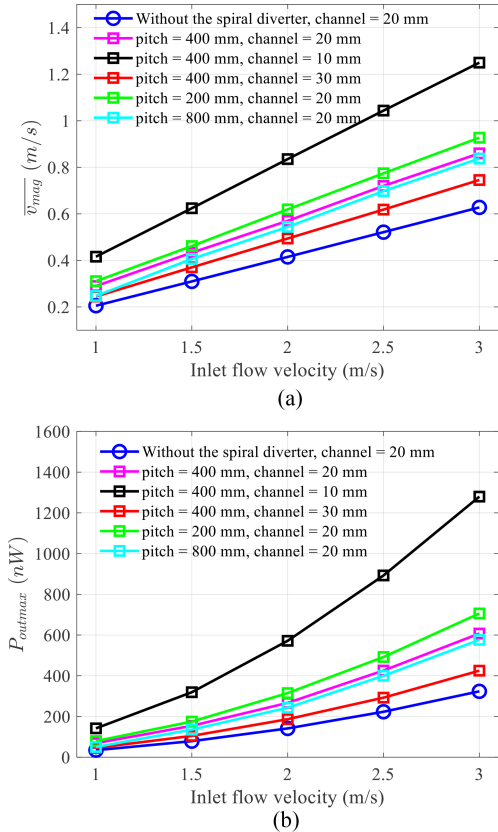


**Fig. 12.** Simulation results. (a) Average flow velocity in the channels. (b) Expected power output.

with the channel width  $c$ . It should be noticed that, with a pitch as small as 200 mm, the turbulence will be much more dominant, and thus, large fluctuation of  $\bar{v}_{mag}$  in these cases is observed in the simulation. Those fluctuations will be transformed into the power output fluctuation. Moreover, the additional mechanical vibration will limit the lifetime of the energy harvester. Thus, very small spiral pitches should be avoided. In this specific application, a spiral flow diverter with a pitch of 400 mm and channel width  $c$  of 10 mm is desired.

In all the cases,  $\bar{v}_{mag}$  increases linearly with the inlet flow velocity. And the theoretical power outputs based on (5) are calculated and shown in Fig. 12(b). Different channel width  $c$  will also change the volume of the flow channel, but the spiral flow diverter with a pitch of 400 mm and channel width  $c$  of 10 mm is still the best.

Fig. 13 shows that, after using the spiral flow diverter with the configuration determined above, the flow velocity is enhanced by approximately 100%, which means that the final power output will be enhanced by about three times according to the model.

### C. Final Design

The final design is shown in Fig. 14. Compared with the conceptual design in Fig. 2, a spiral flow diverter and a magnetic concentrator are integrated into the design.

The flow development part and the tail part are made of any material that can provide enough structural strength, as

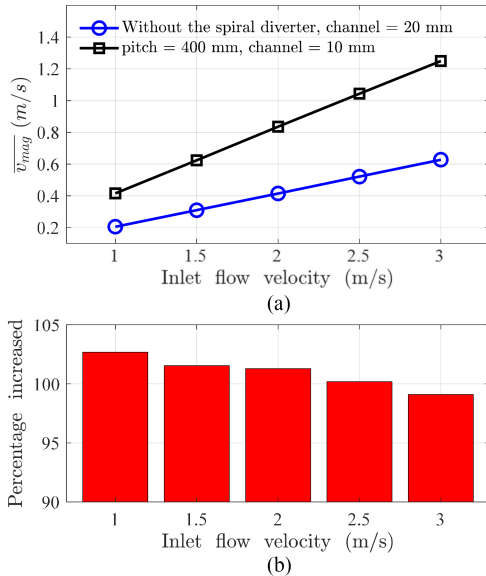


Fig. 13. Flow velocity enhancement. (a) Average flow velocity before and after the optimization. (b) Percentage increase of flow velocity.

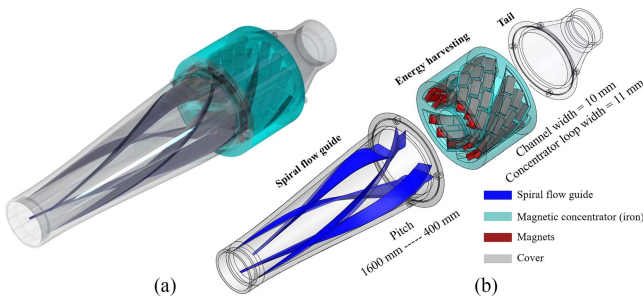


Fig. 14. Final design. (a) CAD rendering. (b) Detailed view of the three parts.

TABLE II  
PROPERTIES OF THE MAGNETS USED

Residual Flux Density	Coercive Force	Intrinsic Coercive Force	Maximum Energy Product
14.5-14.8 KGs	>11.2 KOe	>11 KOe	49.5-52 MGOe

the material will not influence the performance. For the flow development part, the inner diameters of the flow inlet and the flow outlet are 50.8 mm and 105.5 mm, respectively. The length of the flow development part is 340 mm. The dark blue part is the spiral flow guide to stimulate the vortex with a gradually changing pitch from 1600 mm to 400 mm to capture more flow. Even with the spiral flow guide, the center of this part is still a 5.08 cm diameter hollow for robots to travel through. The total length of the tail part is 110 mm, with the same inner diameters on the outlet and inlet as the flow development part.

The energy harvesting part is the middle part in Fig. 14(b). The channel width in the design is 10 mm. The pitch of the energy harvesting part is 400 mm. The cyan part is the magnetic concentrator made with ductile iron with a loop width of 11 mm. The red components are the magnets with properties listed in Table II. The magnets on the outer side for each channel are

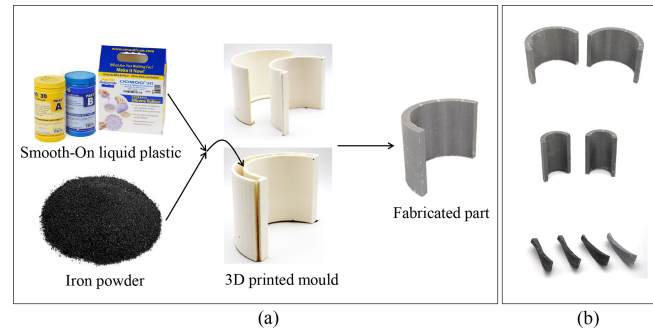


Fig. 15. Plastic casting of the iron parts. (a) Example of the fabrication process. (b) Fabricated iron parts.

organized in an array of  $3 \times 4$  with the size for each magnet of  $25.4 \text{ mm} \times 6.35 \text{ mm} \times 12.7 \text{ mm}$ . The inner layer of magnets is almost the same except that the size of the magnets in the middle line is  $25.4 \text{ mm} \times 6.35 \text{ mm} \times 6.35 \text{ mm}$  due to space limitation.

## V. FABRICATION AND EXPERIMENTS

In this section, we will describe our methods to prototype and test the energy harvester, together with the experimental results and discussions.

### A. Prototyping and Fabrication

In the prototyping process, the whole energy harvester is divided into three parts, as described in Fig. 14(b). Each part is connected with each other using screws and rubber plates in the gap to seal the leak. fused deposition modeling (FDM) 3-D printing is largely adopted in the fabrication of plastic parts to reduce manual effort. The 3-D printer used is Fortus 250mc with a minimum tip size of 0.7 mm and a printing material of acrylonitrile butadiene styrene (ABS).

The flow development part and tail part of Fig. 14(b) are firstly printed and then coated with Flex Seal spray rubber sealant for waterproofing on the inner surfaces.

The most complicated part is the energy harvesting module of Fig. 14(b). Because the shape of the magnetic concentrator is very complicated and severe dead ends occur, traditional machining fabrication methods are not efficient here. Considering a multiaxis CNC is available, it will require significant work to decompose the CAD model and find a way to hold the metal for the machine to mill the spiral surface. A method, very similar to casting, is proposed to fabricate the magnetic concentrator part. The process of the method is illustrated in Fig. 15. First, we mix liquid plastic and iron powder with the same properties as we use in the magnetic simulations. And then, the mixture is poured into the 3-D printed molds. After about 30 min, the 3-D printed molds are removed, and we get the iron concentrator in the shape we desire. The range of the shapes allowed using this method is much wider than traditional machining methods. And it can dramatically increase the production efficiency. The total time for the material to solidify is about 30 min instead of hours when using traditional methods. Moreover, the removed 3-D printed parts can be reused, which means that a lot of material and

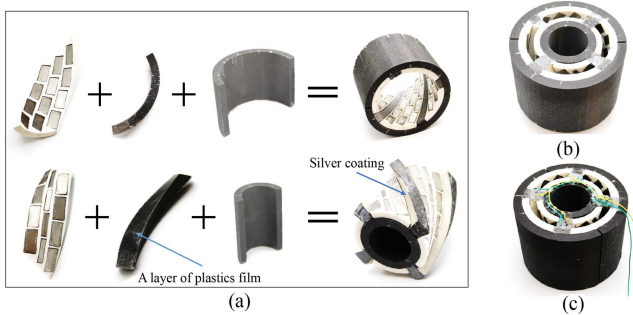


**Fig. 16.** Energy harvesting part assembly. (a) Components and the assembly process. (b) Front view of the energy harvesting part. (c) Back view of the energy harvesting part with cables connected.

printing time can be saved. The process and the parts fabricated are shown in Fig. 15.

After all the iron parts are fabricated, the assembly is conducted. Several magnet housings are 3-D printed. N52 degree Neodymium magnets from K.J. Magnetics are stuck to the magnet housings using the multipurpose super glue from Krazy Glue. The properties of the magnets used are listed in Table II. A thin layer of plastic film is attached to the sidewall of each channel to prevent the conductivity between the two electrodes on the same channel wall. And then, a layer of silver conductive paint from MG Chemicals, working as electrodes with a curved shape, is placed on the plastic film. Nickel and Carbon coating from MG Chemicals are also tested on a sample ABS plate printed using the same setup and machine. However, the carbon paint does not stick well on the surface, and the Nickel coating introduces a much higher inner resistance. Finally, all the components are assembled, as shown in Fig. 16(a), and the final assembled energy harvesting part is shown in Fig. 16(b) and (c).

After assembling all the parts together, the fabrication of the MHD energy harvester is complete. With the similar method, another energy harvester without the magnets and the magnetic concentrator is also fabricated to verify that the power output is not from measurement errors and other effects, such as water level change, flow velocity change, or air bubble amount change.

### B. Experimental Setup

After the fabrication, the MHD energy harvester is tested at the MIT Mechatronics Research Laboratory. The experimental setup and the MHD energy harvester fabricated are shown in Fig. 17(a) and (b). Another energy harvester without magnets and the magnetic concentrator is shown in Fig. 17(c).

The experimental setup of Fig. 17 is composed of a polyethylene tank to hold water, a 1-hp submersible water pump to pump water directly into the 2-inch pipe loop, a ball valve to control the flow rate during experiments, a paddle-wheel flow meter to measure the flow rate, and a test segment with socket unions at the two ends to easily replace the energy harvester to test. Moreover, the pipe loop is fully sectional, achieved by the socket union connections, so that it can be easily adjusted for other experiments of the smart pipe system.

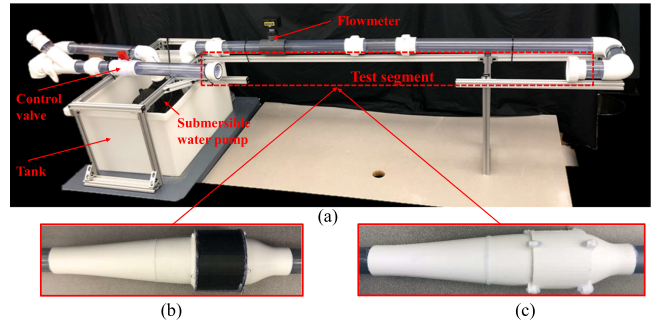


**Fig. 17.** Experimental setup. (a) Water loop for experiments. (b) MHD energy harvester. (c) Energy harvester without magnets and the concentrator.

The conductivity of water is measured by an Ultrameter III 9P from Myron L Company at a temperature of 20.7 °C and after three times of prerinse with sample water. The conductivity of water running directly from the tap is measured to be 0.0750 S/m, while the conductivity of water from the experiment tank is 0.0832 S/m. The electrodes are connected to a programmable load resistor with 1% tolerance. The voltage between the resistor is measured with a Tektronix DPO 2024 digital phosphor oscilloscope to calculate the power output. The pipe is first filled with water and then the pump is turned ON again to produce water flow. The voltage jump is the voltage produced by the energy harvester and extracted by the load resistor.

### C. Experimental Results

The energy harvester without magnets and concentrators is tested first. Under any conditions, the voltage output cannot be noticed on the oscilloscope, and the power output thus cannot be calculated. This indicates that the following power generated with the working MHD energy harvester is valid, not from measurement error or other sources of potential voltage change due to the water level change and the conductor change from air to water.

The voltage output and the power output with an inlet flow velocity of 1.5 and 2 m/s are shown in Fig. 18(a) and (b). The time series of the voltage output under two optimal load resistances are illustrated in Fig. 18(c). After the water pump is actuated, there is an obvious jump in the voltage output. The maximum power output with an inlet velocity of 2 m/s is 87.47 nW with an optimal load resistance of around 550 Ω. The maximum power output for cases with an inlet flow velocity of 1.5 m/s is 58.13 nW with an optimal load resistance at around 650 Ω.

The MHD energy harvester simplified model is verified and validated preliminarily with initial experimental results. Fully verifying the model with this prototype and design is difficult as the flow velocity term within the channels in (5) is hard to measure. However, some other data can provide a preliminary model validation. First, according to (6), the optimal load resistance does not depend on the flow velocity, which agrees well with our experimental results. The optimal load resistance shows a small change for flow velocities of 1.5 and 2 m/s is 650 and 550 Ω, respectively. Second, the experimental results' trends agree well

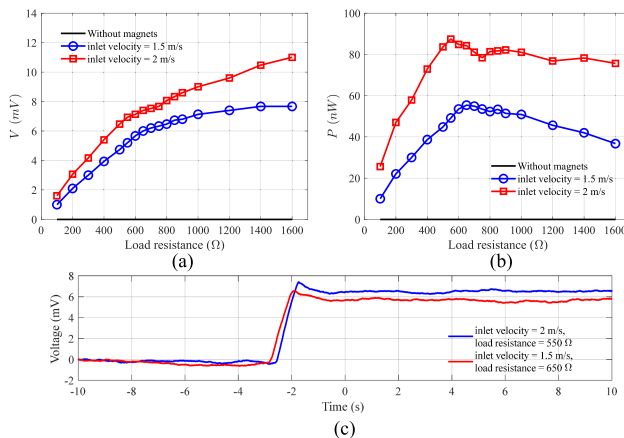


**Fig. 18.** Experimental results. (a) Average voltage output. (b) Average power output. (c) Time series of the voltage output at the optimal load resistance.

with (5) and (6). It is clearly shown that the voltage output increases with the load resistance and flow velocity. And the power output shows a peak at the optimal resistance. However, the trends under the two flow velocities are slightly different in the range with load resistance greater than the optimal value. In this range, the voltage output trend for the cases with an inlet velocity of 1.5 m/s is much flatter than the cases with an inlet velocity of 2 m/s. This results in that power output for the 1.5-m/s working condition decreases much faster with load resistance.

## VI. DISCUSSIONS AND FUTURE WORKS

This article is the first ever working MHD energy harvester using water as a conductor designed for ultralow power sensor networks.

Some other methods in the literature may have the capability to generate more power, but they all have limitations and may not be practical in this application. As discussed in Section I, conventional turbines can generate power ranging from the milliwatt level [35] to sufficient power around several watts [15] for small pipe applications. This is based on the specific requirements of the problem with careful design and tuning of the parameters. Piezoelectricity and electromagnetic methods usually generate power in the order of microwatt or milliwatt [16]–[18], [36]–[40]. However, all these three methods require mechanically moving or vibrating components, which dramatically limit the robustness and lifetime of the device. And the latter two methods also suffer from the off-resonant phenomenon. This means that the power output will decay dramatically if the flow velocity is changed, which is common for water distribution systems. The power output for thermal electricity is dramatically limited by the temperature difference between water and soil, which is around 3 °C [21]. Moreover, the power output of thermal electricity highly depends on weather and location, which makes it challenging to work continuously in this application. The power output of solar energy harvesters highly depends on the size of the solar cells and the environmental conditions. However, it requires tedious placement of devices above the ground and wiring.

Although the power output of the MHD energy harvester is limited now, it has the following benefits:

- 1) Robustness and long lifetime due to no moving components.
- 2) Wide working range of temperatures and flow velocities.
- 3) Local deployment without devices above ground.
- 4) Great potential for integrated power delivery in smart pipes.
- 5) Allows harvested energy to power ultralow-power sensors.

The sensor power requirements, for different applications, are becoming lower and lower. In 2014, Sadeghioon *et al.* [9] developed a leak detection sensor that consumes only 2.2  $\mu$ W. This system uses a power management strategy that operates the sensor node every 6 h. With more aggressive power management systems and MEMS technology, the power requirements can be further decreased to hundreds of nanowatts. Moreover, the rapidly growing capability of machine intelligence can decrease the sensor power requirement. Thus, with the advancement of MEMS, machine learning, and power management, the power requirement will be much lower in the future, as to be satisfied by MHD energy harvesters.

The MHD energy harvester's performance can be improved dramatically in several ways as outlined in this article. The maximum power output is proportional to the channel volume as (5) indicates. Thus, the magnitude of the power output in real applications can be significantly increased. It is important to note that the prototype, presented in this article, has only a 10-cm long energy harvesting device on a 5.08-cm pipe segment. This is due to lab space limitations. In addition, the power can be increased by increasing the magnetic flux density in the channels. This can be achieved by customized magnets. Arc shaped magnets eliminate the gaps between the block magnets and thus provide more flux and the magnetic flux distribution will be more ideal. The current prototype uses block magnets to approximate the twisted arc magnets. Other potential magnetic field and flow field enhancements can be investigated since flow velocity and magnetic flux density both have a quadratic contribution to the power output. For example, some other shapes of the concentrator or the use of metamaterials can be considered. This area is worth careful consideration.

Another aspect of future research can be the modeling of the MHD phenomenon to better guide the optimization process. First, since the channels of the energy harvester are twisted to boost the flow velocity, it makes the validation of the model proposed in Section III difficult. The flow velocity within the channels cannot be measured with the equipments we have in hand. In addition, even though the magnetic flux density at one point can be measured with a Gauss meter, the distribution of magnetic flux density in the channel is significantly nonlinear. Second, a more detailed model considering the amount of bubble, secondary effect, and nonlinearity is still desired even though the trend of the results agrees well with the model as discussed in Section V.

Last but not least, this MHD energy harvester also aims to balance the pressure drop and power output. Another MHD energy harvester we developed earlier, which is shown in Fig. 19,

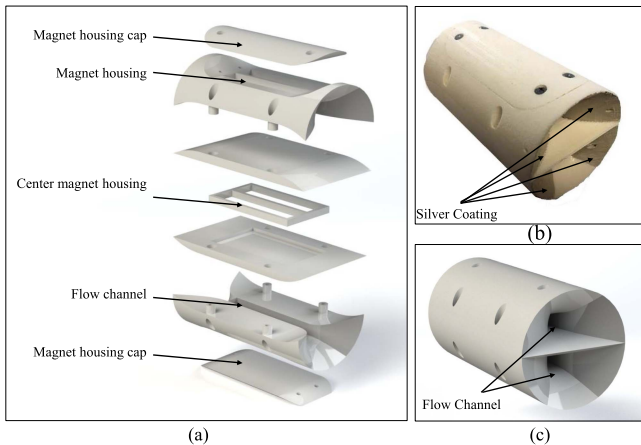


**Fig. 19.** Another high performance design. (a) Explosion view. (b) Real prototype. (c) Rendering.

is tiny and has the ability to generate a 442-nW power output even before integrating a magnetic concentrator [41]. Its length is 15 cm, and the diameter of its cross section is 2 in. This indicates the great potential of MHD energy harvesters in real applications.

Adoption of MHD does present some challenges. The first is the development of a pressure drop within the flow due to the presence of the device. Harvesters extract energy from the water flow and thus cause an additional pressure drop due to energy conservation. Some designs may easily cause a higher pressure drop and possibly a flow blockage making the design impractical. Thus, the balance between power output and pressure drop requires a special consideration. A second challenge is the invasive nature of devices when installed. The modular and sectional MHD design presented here requires cutting the original pipe so the device can be inserted in the pipe system. This is so since the electrodes must contact the conductor, and the conductor's conductivity plays a role. For new pipes, such devices can be integrated in the pipes themselves at the factory. Sensor nodes can also be incorporated into the energy harvester section, and this makes their installation even easier. However, the development of noninvasive MHD energy harvesters is worth investigating. A third challenge is the limited power output. The MHD model presented in this article has a relatively lower power output when compared to other mechanisms. Thus, this MHD design targets the ultralow-power sensors but may not be suitable for applications with high power requirements. Such challenges are, in general, also relevant when considering other applications and future research and development.

## VII. CONCLUSION

A novel MHD energy harvester is developed for low-power sensor networks. A simplified model is proposed and derived first to understand the phenomenon and guide the design and optimization process. It is clearly shown that magnetic flux density and flow velocity are decoupled and both have a quadratic

contribution to the power output. Thus, a carefully tuned magnetic concentrator and spiral flow diverter are integrated into the design to enhance the magnetic flux density and flow velocity, respectively.

The MHD energy harvester is prototyped and tested. The maximum power output at an inlet flow velocity of 2 m/s is 87.47 nW at the optimal load resistance of 550  $\Omega$ . With the experimental results, the simplified MHD model is validated and verified preliminarily. Methods to further enhance the power output is proposed and will be investigated in the future. Last but not least, this article demonstrates the potential of MHD as a promising approach to power wireless sensor networks.

## REFERENCES

- [1] H. Festing *et al.*, CNT, “The case for fixing the leaks: Protecting people and saving water while supporting economic growth in the great lakes region,” 2013. [Online]. Available: [https://www.cnt.org/sites/default/files/publications/CNT\\_CaseforFixingtheLeaks.pdf](https://www.cnt.org/sites/default/files/publications/CNT_CaseforFixingtheLeaks.pdf)
- [2] K. Fukushima, Y. Murata, K. Izumi, Y. Ito, A. Yoshizawa, and T. Tanaka, “A water leak detection service based on sensors and ICT solutions,” *NEC Tech. J.*, vol. 9, no. 1, pp. 107–110, 2015.
- [3] A. O. Lambert, “International report: Water losses management and techniques,” *Water Sci. Technol., Water Supply*, vol. 2, no. 4, pp. 1–20, 2002.
- [4] R. Mamlook and O. Al-Jayyousi, “Fuzzy sets analysis for leak detection in infrastructure systems: A proposed methodology,” *Clean Technol. Environ. Policy*, vol. 6, no. 1, pp. 26–31, 2003.
- [5] H. Aboelinga, M. Saidan, R. Al-Weshah, M. Sturm, L. Ribbe, and F.-B. Frechen, “Component analysis for optimal leakage management in madaba, jordan,” *J. Water Supply: Res. Technol.-AQUA*, vol. 67, no. 4, pp. 384–396, 2018.
- [6] M. Eiswirth *et al.*, “Groundwater contamination by leaking sewerage systems,” *Water Down Under: Groundwater/Surf. Hydrol. Common Int. Papers; Preprints of Papers*, pp. 111–114, 1994.
- [7] S. Srirangarajan, M. Iqbal, H. B. Lim, M. Allen, A. Preis, and A. J. Whittle, “Water main burst event detection and localization,” in *Proc. Water Distrib. Syst. Anal.*, 2010, pp. 1324–1335.
- [8] S. Rathnayaka, B. Shannon, R. Deo, G. Fu, and J. Kodikara, “Failure prevention of large-diameter cast iron water pipes using leak-before-break concept,” in *Proc. Australas. Conf. Mech. Struc. Mater.* 2018, 2020, pp. 677–687.
- [9] A. M. Sadeghioon, N. Metje, D. N. Chapman, and C. J. Anthony, “SmartPipes: Smart wireless sensor networks for leak detection in water pipelines,” *J. Sensor Actuator Netw.*, vol. 3, no. 1, pp. 64–78, 2014.
- [10] M. Carminati *et al.*, “Smart pipe: A miniaturized sensor platform for real-time monitoring of drinking water quality,” in *Proc. IEEE Workshop Environmental, Energy, Struct. Monit. Syst.*, 2017, pp. 1–6.
- [11] D. M. Chatzigeorgiou, Y. Wu, K. Youcef-Toumi, and R. Ben-Mansour, “Reliable sensing of leaks in pipelines,” in *Proc. Dyn. Syst. Control Conf.*, 2013, vol. 56130, Art. no. V00 2T25A004.
- [12] D. Wu, D. Chatzigeorgiou, K. Youcef-Toumi, and R. Ben-Mansour, “Node localization in robotic sensor networks for pipeline inspection,” *IEEE Trans. Ind. Informat.*, vol. 12, no. 2, pp. 809–819, Apr. 2016.
- [13] Y. Wu, A. Noel, D. D. Kim, K. Youcef-Toumi, and R. Ben-Mansour, “Design of a maneuverable swimming robot for in-pipe missions,” in *Proc. IEEE/RSJ Int. Conf. Intell. Robots Syst.*, 2015, pp. 4864–4871.
- [14] S. Folkman, “Water main break rates in the USA and Canada: A comprehensive study,” *Mech. Aerosp. Eng. Fac. Publications*, Paper 174. [Online]. Available: [https://digitalcommons.usu.edu/mae\\_facpub/174](https://digitalcommons.usu.edu/mae_facpub/174)
- [15] M. Casini, “Harvesting energy from in-pipe hydro systems at urban and building scale,” *Int. J. Smart Grid Clean Energy*, vol. 4, no. 4, pp. 316–327, 2015.
- [16] F. U. Qureshi, A. Muhtaroğlu, and K. Tuncay, “Near-optimal design of scalable energy harvester for underwater pipeline monitoring applications with consideration of impact to pipeline performance,” *IEEE Sensors J.*, vol. 17, no. 7, pp. 1981–1991, Apr. 2017.
- [17] G. W. Taylor, J. R. Burns, S. Kamann, W. B. Powers, and T. R. Welsh, “The energy harvesting Eel: A small subsurface ocean/river power generator,” *IEEE J. Ocean. Eng.*, vol. 26, no. 4, pp. 539–547, Oct. 2001.

- [18] A. H. Techet *et al.*, "Piezoelectric eels for energy harvesting in the ocean," in *Proc. 12th Int. Offshore Polar Eng. Conf. Int. Soc.*, 2002, pp. 713–718.
- [19] M. P. S. Dos Santos *et al.*, "Magnetic levitation-based electromagnetic energy harvesting: A semi-analytical nonlinear model for energy transduction," *Sci. Rep.*, vol. 6, no. 1, pp. 1–9, 2016.
- [20] P.-H. Hsieh, C.-H. Chen, and H.-C. Chen, "Improving the scavenged power of nonlinear piezoelectric energy harvesting interface at off-resonance by introducing switching delay," *IEEE Trans. Power Electron.*, vol. 30, no. 6, pp. 3142–3155, Jun. 2015.
- [21] G. Ye and K. Soga, "Energy harvesting from water distribution systems," *J. Energy Eng.*, vol. 138, no. 1, pp. 7–17, 2012.
- [22] D. Dondi, A. Bertacchini, D. Brunelli, L. Larcher, and L. Benini, "Modeling and optimization of a solar energy harvester system for self-powered wireless sensor networks," *IEEE Trans. Ind. Electron.*, vol. 55, no. 7, pp. 2759–2766, Jul. 2008.
- [23] V. K. Sachan, S. A. Imam, and M. Beg, "Energy-efficient communication methods in wireless sensor networks: A critical review," *Int. J. Comput. Appl.*, vol. 39, no. 17, pp. 35–48, 2012.
- [24] B. Thoen, G. Ottoy, and L. De Strycker, "An ultralow-power omnidirectional MEMS microphone array for wireless acoustic sensors," in *Proc. IEEE SENSORS*, 2017, pp. 1–3.
- [25] Y.-S. Lin, D. Sylvester, and D. Blaauw, "An ultralow-power 1-V, 220nW temperature sensor for passive wireless applications," in *Proc. IEEE Custom Integr. Circuits Conf.*, 2008, pp. 507–510.
- [26] M. Faraday, *Philosophical Transactions of the Royal Society of London*, no. 175, 1832.
- [27] V. Malghan, "History of MHD power plant development," *Energy Convers. Manage.*, vol. 37, no. 5, pp. 569–590, 1996.
- [28] S. Chen, H. Chen, D. Martnez, and W. Matthaeus, "Lattice Boltzmann model for simulation of magnetohydrodynamics," *Phys. Rev. Lett.*, vol. 67, no. 27, 1991, Art. no. 3776.
- [29] H. Kobayashi, "Large eddy simulation of magnetohydrodynamic turbulent channel flows with local subgrid-scale model based on coherent structures," *Phys. Fluids*, vol. 18, no. 4, 2006, Art. no. 045107.
- [30] M. Sheikholeslami, M. G. Bandpy, R. Ellahi, and A. Zeeshan, "Simulation of MHD cuo-water nanofluid flow and convective heat transfer considering Lorentz forces," *J. Magnetism Magn. Mater.*, vol. 369, pp. 69–80, 2014.
- [31] Y. F. Yeung and K. Youcef-Toumi, "An in-pipe manipulator for contaminationless rehabilitation of water distribution pipes," in *Proc. IEEE/RSJ Int. Conf. Intell. Robots Syst.*, 2020, pp. 6390–6397.
- [32] R. C. Hughes, P. Mürau, and G. Gundersen, "Ultrapure water. preparation and quality," *Anal. Chem.*, vol. 43, no. 6, pp. 691–696, 1971.
- [33] R. Cox, F. Culkin, R. Greenhalgh, and J. Riley, "Chlorinity, conductivity, and density of sea water," *Nature*, vol. 193, no. 4815, pp. 518–520, 1962.
- [34] K. Elsayed and C. Lacor, "The effect of cyclone inlet dimensions on the flow pattern and performance," *Appl. Math. modelling*, vol. 35, no. 4, pp. 1952–1968, 2011.
- [35] S. Bousseau, A.-B. Duret, M. Perez, E. Jallas, and E. Jallas, "Water flow energy harvesters for autonomous flowmeters," in *Proc. J. Physics: Conf. Ser.*, 2016, vol. 773, Art. no. 012019.
- [36] B. Yang *et al.*, "Electromagnetic energy harvesting from vibrations of multiple frequencies," *J. Micromechanics Microengineering*, vol. 19, no. 3, 2009, Art. no. 035001.
- [37] C. R. Saha, T. O'Donnell, H. Loder, S. Beeby, and J. Tudor, "Optimization of an electromagnetic energy harvesting device," *IEEE Trans. Magn.*, vol. 42, no. 10, pp. 3509–3511, Oct. 2006.
- [38] D.-A. Wang and K.-H. Chang, "Electromagnetic energy harvesting from flow induced vibration," *Microelectronics J.*, vol. 41, no. 6, pp. 356–364, 2010.
- [39] M. Cai and W.-H. Liao, "Design, modeling, and experiments of electromagnetic energy harvester embedded in smart watch and wristband as power source," *IEEE/ASME Trans. Mechatronics*, vol. 26, no. 4, pp. 2104–2114, Aug. 2021.
- [40] H. J. Jung, A. T. Eshghi, and S. Lee, "Structural failure detection using wireless transmission rate from piezoelectric energy harvesters," *IEEE/ASME Trans. Mechatronics*, vol. 26, no. 4, pp. 1708–1718, Aug. 2021.
- [41] X. Zhang, "Design and optimization of an MHD energy harvester for intelligent pipe systems," Ph.D. dissertation, Dept. Mech. Eng., Massachusetts Inst. Technol., 2019.



**Xiaotong Zhang** (Graduate Student Member, IEEE) received the B.S. degree in naval architecture and ocean engineering from Shanghai Jiao Tong University, Shanghai, China, in 2017, and the M.S. degree in mechanical engineering from the Massachusetts Institute of Technology (MIT), Cambridge, MA, USA, in 2019. He is currently working toward the Ph.D. degree in instrumentation, perception, and planning for autonomous agents and robots with the Mechatronics Research Laboratory, Department of Mechanical Engineering, MIT.

His research interests include mechatronics, instrumentation, automation, and robotics in the aspects of both hardware and software.



**Kamal Youcef-Toumi** (Senior Member, IEEE) received the B.S. degree in mechanical engineering from the University of Cincinnati, Cincinnati, OH, USA, in 1979, and the M.S. and Sc.D. degrees in mechanical engineering from Massachusetts Institute of Technology (MIT), Cambridge, MA, USA, in 1981 and 1985, respectively.

His research interests include modeling, design, instrumentation, and control systems theory and their applications to dynamic systems.

Mr. Youcef-Toumi is a fellow of the American Society of Mechanical Engineers.